EFFECT OF GRAPHENE NANOFLAKES ON THE STRUCTURAL, MECHANICAL, AND ELECTRICAL PROPERTIES OF ACRYLONITRILE BUTADIENE STYRENE

By

WENHAO ZHOU

A thesis submitted to the

School of Graduate Studies

Rutgers, The State University of New Jersey

In partial fulfillment of the requirements

For the degree of

Master of Science

Graduate Program in Material Science and Engineering

Written under the direction of

Jennifer Lynch

And approved by

_____

_____

_____

New Brunswick, New Jersey

January, 2020

ABSTRACT OF THE THESIS

EFFECT OF GRAPHENE NANOFLAKES ON THE STRUCTURAL, MECHANICAL, AND ELECTRICAL PROPERTIES OF ACRYLONITRILE BUTADIENE STYRENE

By WENHAO ZHOU

Thesis Director:

Jennifer Lynch

Acrylonitrile butadiene styrene (ABS) is a common thermoplastic polymer used in engineering, electrical, textile, and automotive industries. ABS has good impact resistance and toughness but suffers from low flexural modulus and strength. Typically, ABS is mixed with other materials to create a composite with better properties. In this work, graphite was exfoliated into graphene nanoflakes (GNFs) within ABS in concentrations of 1, 5, and 20 wt.% GNFs followed by injection molding to fabricate GNF-ABS specimens for testing. The morphology and structure of the GNF-ABS composites were characterized using scanning electron microscopy (SEM), X-ray diffraction (XRD), Raman spectroscopy. And X-ray photoemission spectroscopy (XPS). The mechanical properties in flexure and electrical conductivity of the GNF-ABS composites were also determined. Results show that GNF particles created within ABS are multilayer graphene, and that increasing GNF concentration increases flexural modulus and strength, as well as impart electrical conductivity.

Acknowledgments

First of all, I am very grateful to my mentor, Dr. Lynch, for her careful guidance of my graduation thesis in the past year, which greatly improved my understanding of academic writing and taught me a lot of specific research skills. I am also grateful to Ali Ashraf, and Elizabeth Chang, whose technical and moral support helped me get through the more difficult parts of my Master. Thanks to my friends who have given me care and support in life, because of you, the university life is colorful. Finally, I would like to thank my parents for their unconditional love and endless emotional supports.

Dedication

I would like to dedicate this work to my parents and all of my friends.

Table of contents

List of Tables

List of Figures

1 Chapter 1: Introduction

To improve the performance of a polymers, reinforcing agents are added to fabricate polymer-based composite materials. A thermoplastic composite is prepared by melt-blending a filler, reinforcement, or functional material within a polymer matrix. Application areas of these composites include aerospace, automotive, chemical industries, etc. In this work, graphite is converted into graphene nanoflakes (GNFs) directly within acrylonitrile butadiene styrene (ABS) using a uniform shear melt-processing method and resulting in G-ABS composites.

1.1 Acrylonitrile Butadiene Styrene (ABS)

ABS is a common thermoplastic used for its light weight, high impact resistance, toughness, chemical resistance and so on. However, it has poor flame resistance and flexural strength. So many other polymers, metals, or reinforcing agents are often combined into the ABS production to improve properties.

ABS is developed on the basis of polystyrene modification. Before ABS appeared, US Rubber company and producers of polystyrene studied the use of styrene butadiene rubber and nitrile rubber to improve the brittleness of styrene. In 1947, the American Rubber Company first prepared ABS by using blending method. In 1954, the US Borg-Warner Corporation introduced ABS to commercial markets. Nowadays, graft emulsion polymerization is the most popular method in industry to produce ABS. This method has the most mature process, and it is the most practical ABS production method.

The development trend of ABS is to develop high-performance, multi-functional

special polymer to increase the added value and market competitiveness of products. High-performance ABS mainly include heat-resistant ABS, weather-resistant ABS, high-impact ABS, transparent ABS, high-gloss ABS, flame-retardant ABS, conductive ABS, antistatic ABS, etc.

As shown in Figure 1.1, ABS is combined by three major components, and the final properties are dependent on the ratio of each component. The acrylonitrile is responsible for chemical resistance and thermal stability. The butadiene contributes to the toughness and impact strength. The styrene is the cause of stiffness and processability.

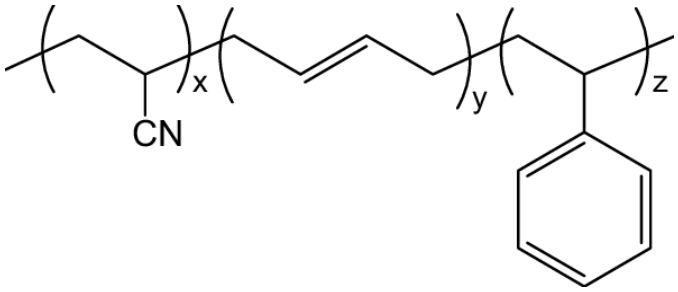

Figure 1.1 Structure of Acrylonitrile butadiene styrene.

1.2 Graphite

Graphite is an allotrope of carbon, which has high thermal stability, electrical and thermal conductivity, chemical stability, plasticity and lubricity. It is widespread used as electrodes, fibers, lubricant and so on.

As shown in Figure 1.2, Graphite is defined as a layered structure composed of infinitely large planar layers of carbon hexagons. The carbon in graphite is sp2 orbital hybrids and the atoms form in planes with each covalently bound to three nearest neighbors 120 degrees apart. There are secondary bonds between the layers.

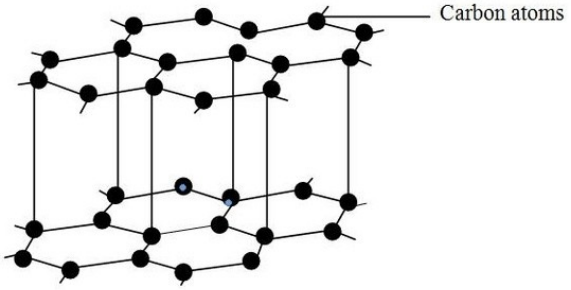

Figure 1.2 Structure of graphite

1.3 Research background

Recently, there are many researches presenting reinforcement of Acrylonitrile butadiene styrene (ABS) with many kinds of materials. A. Shenavar used carbon black (CB) as reinforcement with ABS [1] and showed that increasing the CB content in the composite can increase the thermal stability and decrease the impact strength. H.E.Mayasari also claimed that CB is a good filler for ABS to reach a good thermal stability and swelling resistance [2].

Carbon nanotube (CNT), another kind of allotrope of carbon, is also used as a filler to reinforce the properties of polymers. Jeevan Jyoti's work implied that dynamic moduli and viscosity increased with the addition of CNT in ABS matrix [3].D. Mari's research showed that the glass transition temperature of ABS increased due to the interaction between CNT and ABS[4].

Graphite, the thermodynamically most stable form of carbon, is a material which has good heat and electrical conductivity. B. Ben Difallah studied the effects of graphite in ABS on the mechanical and tribological properties [5]. Their work showed that with the

addition of graphite to the ABS, the elastic modulus and the failure strain decrease significantly. And 7.5 wt. % graphite in ABS contributed best to the friction and wear abilities.

Graphene, a 2D carbon structure which has good electronic and mechanical properties. Cheol Heo used solution-intercalation method to make C18-Graphene/ABS films and results showed that functionalized graphene is sufficient to improve the thermal and tensile properties of ABS films [6].

S. Dul's work investigated effect of graphene nanoplatelets in ABS. In the work, they used four types of commercial graphene nanoplatelets (XG Sciences xGnP M5, C300, C500, and C750). The results indicated that M5 graphene nanoplatelets were the most sufficient to reduce resistivity and improve mechanical properties [7].

Andrea Caradonna studied the effect of graphene nanoplatelets in ABS on thermal properties. The work indicated that graphene nanoplatelets is efficient to increase the thermal conductivity of ABS. But it did not increase the thermal stability [8].

Rupinder Singh' work focused on thermal and electrical conductivity of ABS/Graphene. It showed that by increasing the concentration of graphene in ABS, mechanical, electrical, and thermal properties of ABS composite can be increased [9].

2 Chapter 2: Experimental methods

2.1 Materials

The materials used to prepare the polymer composite studied in this work include graphite and ABS. The graphite is mined flake graphite, and the ABS is Terluran GP-22. Using in situ shear exfoliation, graphite is converted to GNFs directly within ABS during a unique melt processing method. Graphite and ABS were melt-processed between a temperature range of 221 – 267 °C at concentrations of 1, 5, and 20 wt. % graphite in ABS, pelletized, and injection molded to fabricate G-ABS test specimens.

2.2 Injection Molding

Injection molding is a fast and efficient molding method. It is an automatic operation that can easily mold complex shapes, has a wide range of product size, and high dimension accuracy. Injection molding is used for large quantities of production and complicated shapes.

The first injection molding machine was invented by John Wesley Hyatt and Isaiah in 1872 [10]. In 1946, the first screw injector was made by James Watson Hendry. He made it more precise to control the speed and quality of the products [11]. In the 1970s, Hendry developed the first gas-assisted injection molding process which allowed the production of complex, hollow products to cool rapidly. This technology increases the design flexibility mean while reducing the time, cost, and waste of production [12].

The Figure 2.1 shows a common injection molding machine. It has three parts, including injection unit, mold assembly, and clamping unit. The process of injection

molding is called injection molding cycle. This cycle includes five steps. In the first step, the clamping unit closes the mold. In the second step, material in the hopper is fed into the heated barrel as set by the shot size followed by injection under pressure into the mold. During the third step, the hold pressure ensures that enough material is in the mold to avoid part shrinkage. During the fourth step, the mold remains closed to allow the molten material in the mold to cool and solidify. During the cooling, the material may shrink a little, especially semicrystalline polymers. The last step is part ejection. Then, the screw retracts to allow new material ready for injection and the cycle starts again [13].

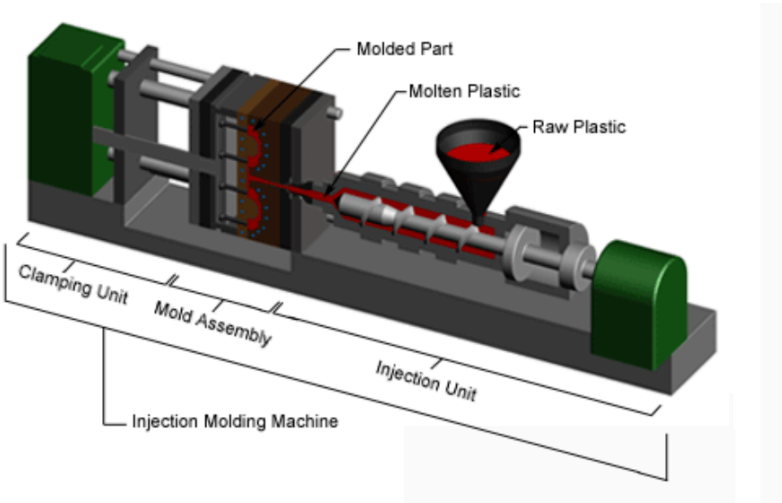

Figure 2.1. Construction of injection molding machine

In this work, graphite was melt-blended with ABS in concentrations of 1, 5, and 20 wt. % graphite using a proprietary uniform, high shear method to exfoliate graphite into GNFs within ABS. The compounded G-ABS composites were pelletized and injection molded using a Negri Boss V55-200 injection molding machine to fabricate testing specimens of 1, 5, and 20 wt. % GNFs in ABS with dimensions 3.5 x 12.5 x 165 mm

(Figure 2.2).

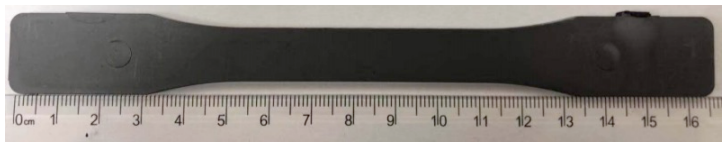

Figure 2.2. Injection molded G-ABA specimen with dimensions 3.5 x 12.5 x 165 mm

2.3 X-ray Diffraction

X-ray Diffraction is a technique used to determine the atomic and molecular structure of a crystal. Crystal structure makes incident X-rays diffract into many specific directions. By measuring these diffracted beams' angles and intensities, crystallographer can make a 3D picture of the density of electrons within the crystal. According to this electron density, the mean positions of the atoms in the crystal, chemical bonds, and other information are determined.

X-rays are electromagnetic radiation that generated by the transition of atoms' inner electrons which under the impact of high-speed moving electrons, mainly including continuous X-rays and characteristic X-rays. Crystals are used as gratings for X-rays, and the coherent scattering produced by these large numbers of particles (atoms, ions, or molecules) will interfere with light, thereby increasing or decreasing the intensity of the scattered X-rays, this phenomenon called constructive or destructive interference. The constructive interference only happens in a few specific directions, determined by Bragg's law, as shown in EQ 2.1 and Figure 2.3.

$$2d\sin\theta = n\lambda \tag{2.1}$$

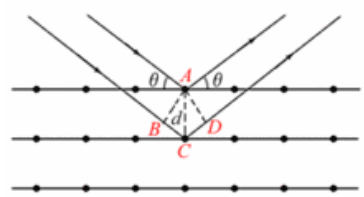

Figure 2.3 Bragg diffraction

Here d is the spacing between diffracting planes, θ is the incident angle, n is any integer, and λ is the wavelength of the beam. d can be calculated by measuring the angle θ. The mean size of the crystalline domains (D) is calculated using the Scherrer equation, shown in EQ 2.2, where K is a dimensionless shape factor with a typical value of about 0.89, λ is the X-ray wavelength, β is the full width at half maximum (FWHM) in radians, and θ is incident angle [14]. From EQ 2.1 and 2.2, the number of graphene layers (n) can be determined, as shown in EQ 2.3 [15].

$$D = \frac{K\lambda}{\beta cos\theta} \tag{2.2}$$

$$n = D/d \tag{2.3}$$

In this work, the XRD analysis of the GNF-ABS nanocomposites was performed using a Panalytical X'pert, with Cu-kα radiation ($\lambda = 1.54059$ Å), operating at 45 kV and 40 mA at a scan rate of $0.02^{\circ}\ s^{-1}$ in a range of 2θ from 5° to 70°. The samples were cut into 35 mm x 13 mm x 3.5 mm. The specimens were fixed on the XRD bulk sample holder by clay. Then using glass slide to press the sample to make the sample and sample holder are in the same level.

2.4 Raman spectroscopy

Raman spectroscopy is based on the Raman scattering effect discovered by C. V. Raman. It obtains vibration and rotation information of molecules from the scattering spectrum and provides a structural fingerprint by which molecules can be identified.

Raman scattering is one kind of inelastic scattering. The source usually comes from laser in the visible, near infrared, or near ultraviolet range. When the laser light interacts with molecular vibrations, phonons or other excitations in the system, the energy of the laser photons will be increased or decreased. This energy shift gives information about the vibration modes.

Raman spectroscopy provides many important information about the structure of polymeric materials. Such as molecular structure and composition, stereoregularity, crystallization and orientation, molecular interactions, and surface and interface structures. From the width of the Raman peak, the stereochemical purity of the polymer material can be characterized. For example, a sample with a random structure sample, the Raman peak is weak and wide, and the highly ordered sample has a strong and sharp Raman peak.

In this work, Raman spectra were obtained using a Renishaw 537L07 microscope. A laser wavelength of 532 nm and spectrum range of 1256-2831 nm were used. Specimen dimensions were 64 mm x 13 mm x 3.5 mm, and data was collected at five points on each specimen. Raman spectroscopy is used to study the structure of graphite and graphene. Typically, graphite shows peaks labeled D, G, and 2D occurring at 1350, 1582, and 2685 cm^{-1}, respectively. The D band is attributed to the induced disorder mode which is caused

by structural defects. The G band and 2D band correspond to the first order scattering of the E_{2g} vibration mode and the second order phonon modes, respectively [16]. The number of graphene layers in the GNF particles is determined by the ratio of the peak intensities of the 2D and G bands, as shown in EQ 2.4. When n~2, it is single layer graphene; when n~1, it is bilayer graphene; when n~0.8, it is few-layer graphene; and when n~0.5, it is multi-layer graphene [17].

$$n = I_{2D}/I_G \tag{2.4}$$

2.5 X-ray Photoelectron Spectroscopy

X-ray photoelectron spectroscopy is an instrument that can measure the chemical state of an element within the surface of the film or a few nanometers below the surface. The instrument consists of several components such as vacuum system, sample introduction system, ion gun, detector, and energy analyzer. A photon (E=hv) is emitted to the surface of the sample through the ion gun, and the electrons in the inner layer of the sample absorb the energy of the photon. When the energy of an electron exceeds the binding energy, the electron will be ejected into the vacuum. This electron is called photoelectron, and the transition process is called Einstein photoelectric effect. XPS obtains a photoelectron spectrum by measuring the kinetic energy of the transition photoelectrons. Through analyzing the position and intensity of the peaks in the spectrum, the elements in the sample and their relative contents are calculated. The change of the chemical bond and the valence state of the element are also determined by the change of the binding energy of the

photoelectron.

When an x-ray photon impinges on a material, it imparts its energy (hν) to a single electron [18]. The electron binding energy is E_b, work function ϕ_{sample}, and the electron's kinetic energy is $E_k{}'$ [19]. Through the Einstein photoelectric effect, hν is defined in EQ 2.5. When the photoelectrons enter the detector, their Fermi levels are equilibrated, as shown in EQ 2.6, where E_k is the kinetic energy of electron measured by the detector. Solving EQ 2.5 and 2.6 for E_k, we get EQ 2.7.

$$hv = E_b + E_k' + \phi_{sample} \tag{2.5}$$

$$E_k' + \phi_{sample} = E_k + \phi_{detector} \tag{2.6}$$

$$E_k = hv - E_b - \phi_{detector} \tag{2.7}$$

In the test, the detector work function is corrected by using a clean gold or silver sample. This method can make sure that Fermi energy lies at 0 eV. A schematic of the binding energy of electrons is shown in Figure 2.4.

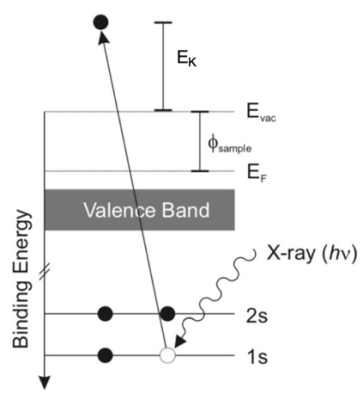

Figure 2.4 Schematic of the photoemission process

Each element has a specific electron binding energy, which is represented in the energy

spectrum as a characteristic line. Therefore, it is possible to determine the specific element by comparing the position of the characteristic line with the position of the standard picture, but H and He cannot be identified by this method. And an accurate spectrum can identify all the elements contained in the sample at once.

There are two ways to calculate the content of the elements. One is calculated by the area of the peaks in the photoelectron spectrum, and another one is to use the standard samples for comparison to determine the content of the elements. Both methods can accurately measure the element content, but the second method is more practical and easier.

In this work, XPS analysis of the GNF-ABS was performed using a ThermoFisher K-Alpha instrument, and X-ray was produced by a monochromatic Al Kα source with a photon energy of hν = 1486.7 eV. Samples were cold fractured in liquid nitrogen using a chisel and hammer to break the specimen into smaller pieces appropriate for XPS testing.

2.6 Scanning Electron Microscope

Scanning Electron Microscopy (SEM) is a microscopy which scans the sample with a very narrow electron beam. The electron beam will interact with the sample and sample will emit the secondary electrons and backscattered electrons. By detecting the secondary electrons and backscattered electrons, we can observe the surface morphology of the sample [20].

Scanning electron microscopy has many advantages as compared with optical microscopy. SEM has a high magnification, and it is continuously adjustable between 2000 and 20000 times. It has a large depth of field, a large field of view, a three-dimensional

image, and can directly observe the structure of the uneven surface of samples. Therefore, it is a very useful scientific research instrument.

When an incident electron impacts with an atom, the incident electron's direction and energy will be changed. This phenomenon is called scattering. According to whether the energy in the scattering changes, it is divided into elastic scattering and inelastic scattering. If the electron only changed direction and the energy did not change, it is elastic scattering. If the direction and energy both changed, it is inelastic scattering. The energy lost by electrons in inelastic scattering is converted into heat, light, X-rays, secondary electrons, etc. Inelastic scattering of electrons is the basis of scanning electron microscopy.

The secondary electron is an electron that is bombarded by the incident electron beam and leaves the surface of the sample [20]. Secondary electrons have lower energy, generally no more than 50 eV, and most secondary electrons only carry a few volts of energy. Secondary electron is generally emitted in the depth range of 5-10 nm of surface, so it is very sensitive to the surface topography of the sample. Therefore, the surface topography of the sample can be displayed very efficiently.

Backscattered electrons are a part of incident electrons reflected from the nucleus in a solid sample [20]. Backscattered electrons are emitted from depth between 100 nm~1μm, so the resolution of backscattered electron images is less than secondary electron images. The intensity of backscattered electron signal increases as the atomic number Z increases and is approximately $I \propto Z^{\frac{2}{3}\sim\frac{3}{4}}$. Therefore, backscattered electrons can not only analyze the topographical features, but also can be used for qualitative component analysis.

The inner electrons of the sample's atoms are excited by the incident electrons, and they are in an excited state with higher energy. At this time, the outer electrons will transport to the inner layer. Thereby X-rays with characteristic energy will be released.

The X-ray will be emerged from 0.5μm~5μm under surface. Wavelength λ follows Moseley's law (EQ 2.8) [21]:

$$\lambda \propto \frac{1}{(Z-\sigma)^2} \tag{2.8}$$

Using the wavelength or energy of characteristic X-rays, it is easy to identify the elements and map their distribution. This method is called Energy-dispersive X-ray spectroscopy or Wavelength-dispersive X-ray spectroscopy

In this work, SEM was performed using Zeiss Sigma FESEM. Specimens were cold fractured in liquid nitrogen and coated with gold to enhance the conductivity using EMS 150T ES Coater. For 1 and 5 wt. % GNFs in ABS, a 20 nm gold coating was applied. For 20 wt. % GNFs in ABS, a gold coating of only 5 nm was applied, since the 20 wt. % GNFs impart conductivity to ABS.

2.7 Electrical Conductivity

The source measure unit (SMU), shown in Figure 2.5, is an electronic instrument which can help us to detect materials' electrical properties. It can do sourcing and measuring at the same time. In the test, this instrument can apply voltage or current accurately and measure accurate voltage and current at same time. SMU is used in test applications that require high precision, high resolution and measurement flexibility. Such applications involve I-V characterization, semiconductors test and some non-linear devices or materials

in which the voltage and current sources have both positive and negative values. To satisfy this, SMU has a four-quadrant output [22].

Figure 2.5 Source measure unit

Resistance can be calculated by using SMU and EQ 2.9 to calculate the volume resistivity, where R_v (Ω) is volume resistance, A (cm^2) is area of the electrodes, and t (cm) is distance between the electrodes. Conductivity is calculated by EQ 2.10 [23]:

$$\rho_v = R_v \frac{A}{t} \tag{2.9}$$

$$\sigma_v = \frac{1}{\rho_v} \tag{2.10}$$

In this work, electrical conductivity test was performed using a 2450 Source Meter UNIT with an applied voltage of 0 to 100 Volts and time of electrification of measurement is 4 s. Measurements were performed at room temperature of ~24° C and humidity of ~60%. As shown in Figure 2.6, specimens were taken from positions A, B, C along sample length and cut into 12.5 mm x 12.5 mm x 3.5 mm specimens. Silver paint was used on two opposing sides of the sample for measurement. Conductivity measurement direction was parallel to flow direction.

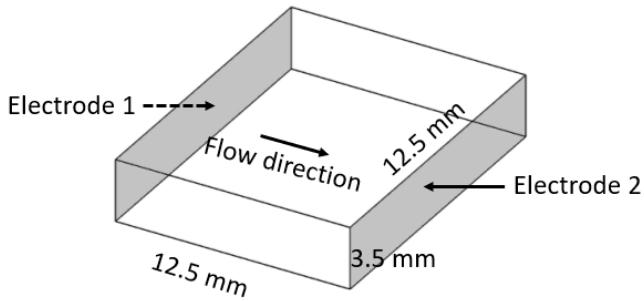

(a)

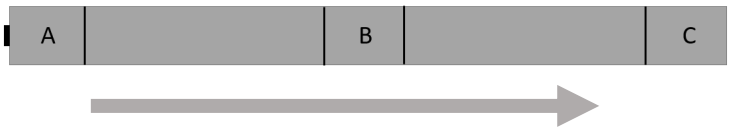

Flow direction
(b)

Figure 2.6 structure of (a) specimen and (b) sample.

2.8 Flexural testing

Flexural testing is generally used to determine the mechanical properties in bending mode, including flexural modulus and flexural strength of the material. Flexural testing in three-point loading is performed by placing a specimen on two supports and one loading anvil placed midway between the supports. In a flexure test, there is a tensile stress in the convex side of the specimen and compression stress in the concave side. But this will create a shear stress along the midline. In a flexure test, we should make sure that primary failure comes from tensile or compression stress, so it is important to decrease the shear stress. The span-to-depth ratio of 16:1 can be used for most materials to minimize the shear stress. Flexural strength is defined as the maximum stress of the outermost fiber and flexural modulus is calculated from the slope of the stress versus strain curve.

In this work, MTS QTest 25 was used for three point loading flexural testing with a 500 N load cell, cross head speed is 1.45 mm/min, according to ASTM D790. Five specimens per concentration were tested and results averaged.

3 Chapter 3: Results and Discussion

3.1 XRD Results

XRD analysis results for 1, 5, and 20 wt.% GNF in ABS is shown in Figure 3.1. Peaks at diffraction angle of 26.5º and 54.6º correspond to (002) and (004) direction and are the typical peaks associated with graphite, as shown in Figure 3.1(a). As the concentration of graphene increased, the intensity of peaks increased. It is easily found that there is a peak at 28.6º, this peak was caused by oxidation of graphite [24]. By using Bragg's law and Scherrer's equation, distance between graphene layers and graphite crystallite sizes can be calculated, and they are shown in Table 3.1 as d and D. Number of graphene layers was calculated by D/d. It is apparent that 20 wt.% GNFs in ABS has smaller grain size and less graphene layer in the GNF particles, also shown graphically by line broadening of the peak at the (002) reflection in Figure 3.1(b).

Table 3.1 Comparison of structural parameters of 1, 5, and 20 wt.% GNF-ABS resulting from the XRD patterns. Notation: d-distance between graphene layers, D-crystallite size of graphene layers, n-number of Graphene Layers.

Samples	d (Angstroms)	D (Angstroms)	n
1G-ABS	3.365	347.9	103.4
5G-ABS	3.366	344.9	102.5
20G-ABS	3.359	284.2	84.6

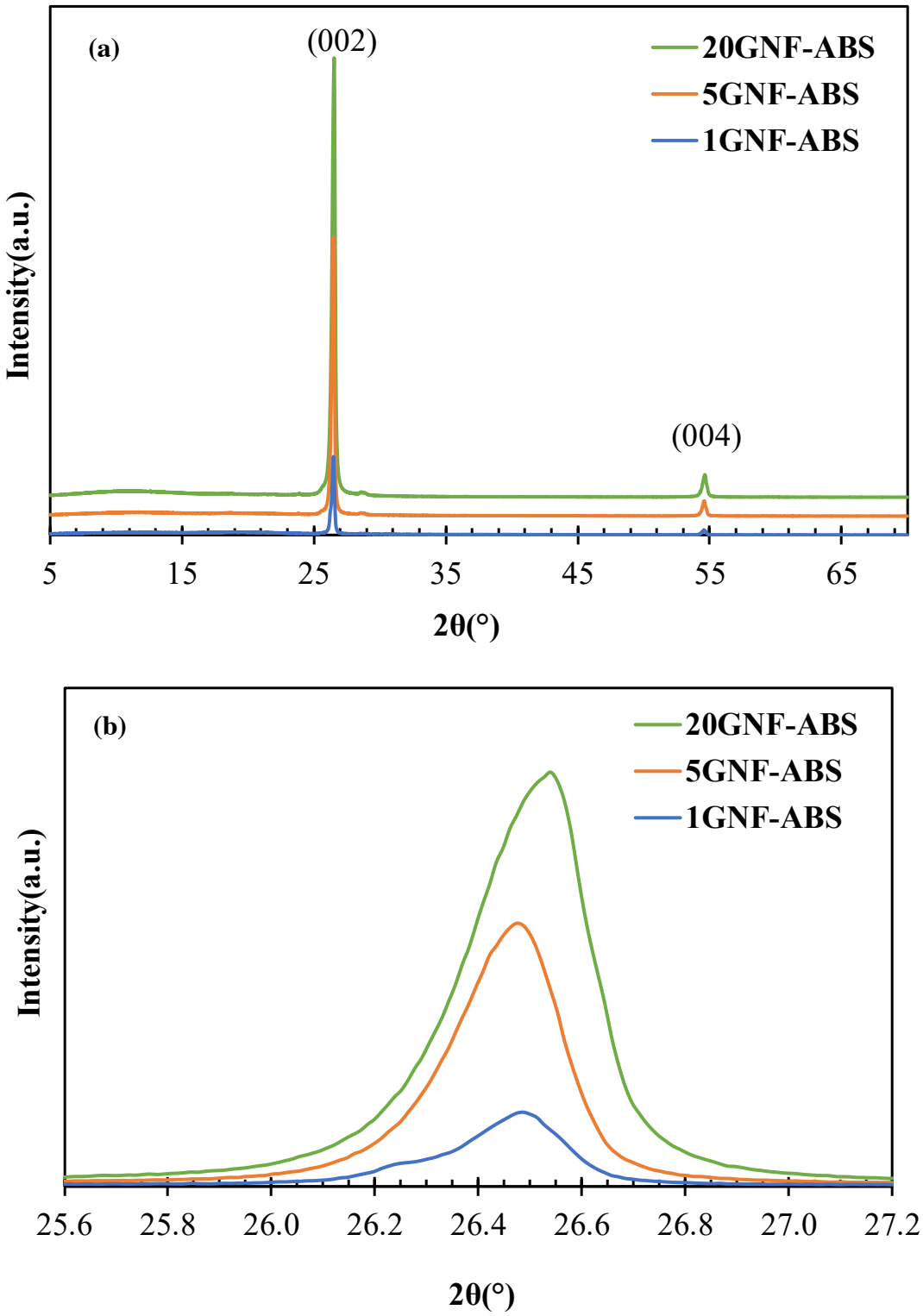

Figure 3.1 XRD pattern of 1, 5, and 20 wt.% GNF in ABS (a) full scale) and (b) area of interest around the (002) reflection of graphite

3.2 Raman Results

In the Raman spectra, the D band determined disorder and defects of the sp^2 carbon ring. The G band and 2D band are exhibited by the graphite. 2D band is always used to determine graphene layer thickness. 2D band split from single peak into several overlapping peaks means that layers of graphene increasing and symmetry lowering in the sample [13]. And I_{2D}/I_G is also used for graphene layer thickness determine. As shown in Figure 3.2 and Table 3.2, peak splitting occurred at 2D band, and the I_{2D}/I_G ratio is approximately 0.5 for 1, 5, and 20 wt.% GNFs in ABS. This suggests that GNF particles in 1, 5, and 20 wt.% GNFs in ABS are all multi-layer graphene.

Table 3.2 I_{2D}/I_G ratio of 1, 5, 20 wt.% GNF in ABS

Samples	I_{2D}/I_G
1GNF-ABS	0.51
5GNF-ABS	0.45
20GNF-ABS	0.52

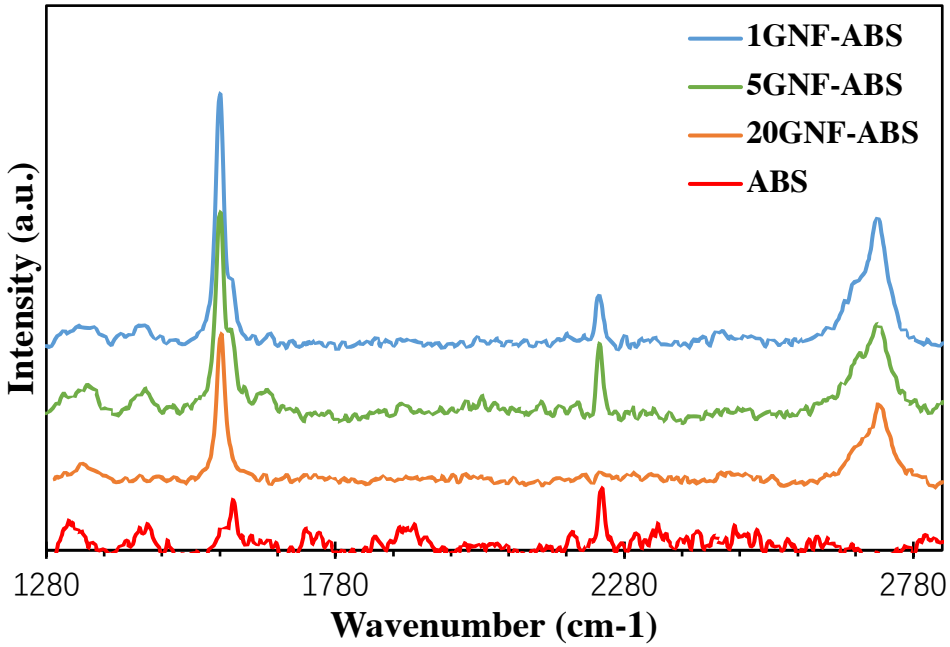

Figure 3.2 Raman spectra of 0, 1, 5, and 20 wt.% GNFs in ABS.

3.3 XPS Results

XPS spectra for 1, 5, and 20 wt. % GNFs in ABS is shown in Figure 3.3. The blue peak corresponds to the C1s peak and was fit with the components shown. The sp2 peak corresponds to carbon-carbon bond in the sp2 carbon ring, defective carbon corresponds to point defect in the carbon ring, and disordered carbon corresponds to two carbon rings that were not in the same plane. The binding energy corresponding to sp2 carbon, defective carbon, and disordered carbon peaks are 284.3 eV, 283.9 eV, and 284.7 eV, respectively. From Figure 3.3 and *Table 3.3*, it is easy to see that as the concentration of GNF increased, sp2 carbon increased and defective carbon decreased, while disordered carbon concentration did not change too much. This result indicates that increasing GNF concentration is helpful for reducing defects during mixing with ABS.

Table 3.3 Elemental composition (atomic %, based on XPS data) of 1, 5, 20 wt.% GNFs in ABS.

Species (Atomic %)	1GNF-ABS	5GNF-ABS	20GNF-ABS
sp2 (284.3 eV)	21.34	23.58	39.38
Defective (283.9 eV)	17.67	17.67	7.13
Disordered (284.7 eV)	26.51	23.28	26.26

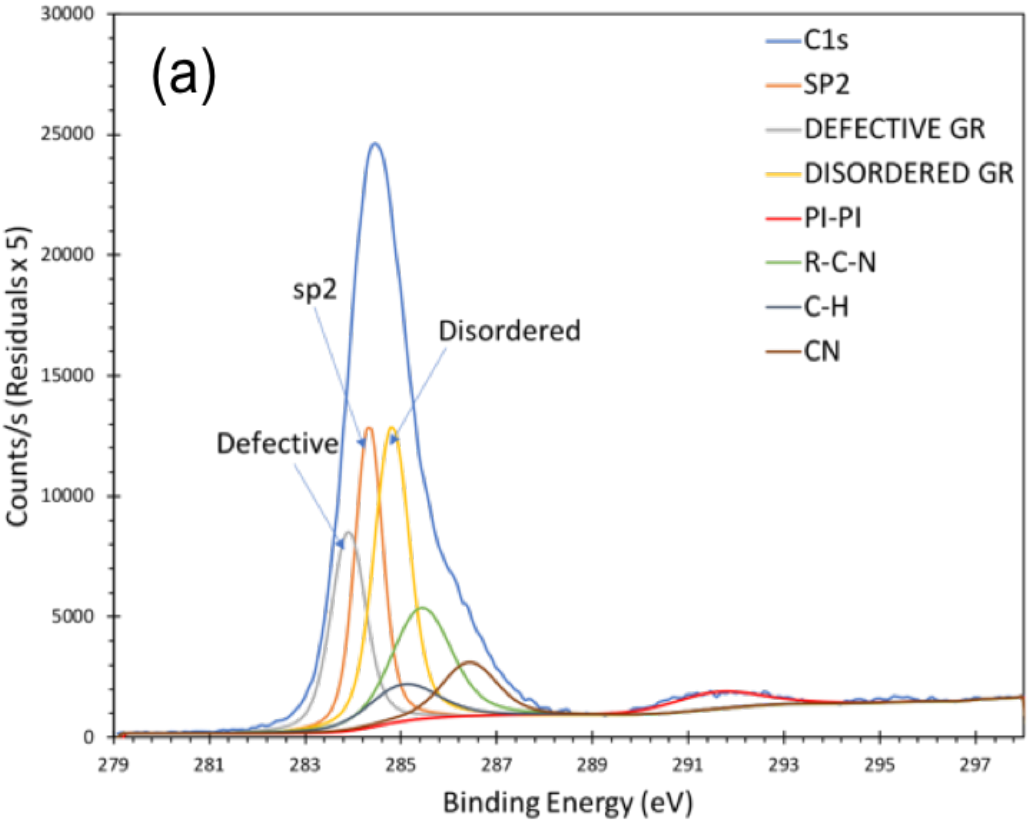

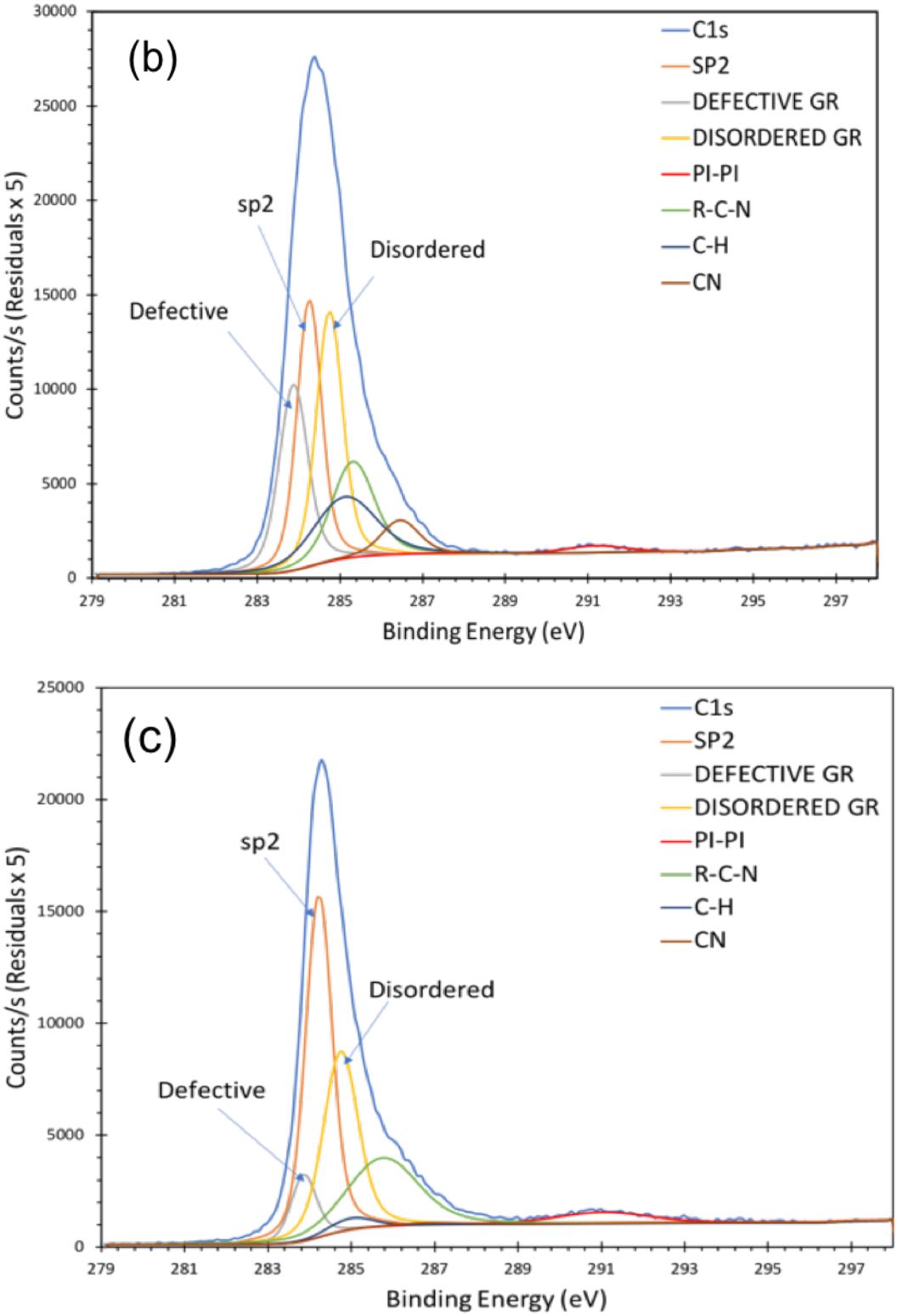

Figure 3.3 XPS C1 spectra of (a) 1GNF-ABS, (b) 5GNF-ABS, (c) 20GNF-ABS.

3.4 SEM Results

The morphology of 1, 5, and 20 wt. % GNFs in ABS is shown in Figure 3.4 at scales of 10 μm and 1 μm. At the lower magnification and 10 μm scale (a, c, e), micrographs show good GNF distribution within ABS. At higher magnification and 1 μm scale (b, d, f), micrographs indicate good particle-matrix interaction between GNFs and ABS.

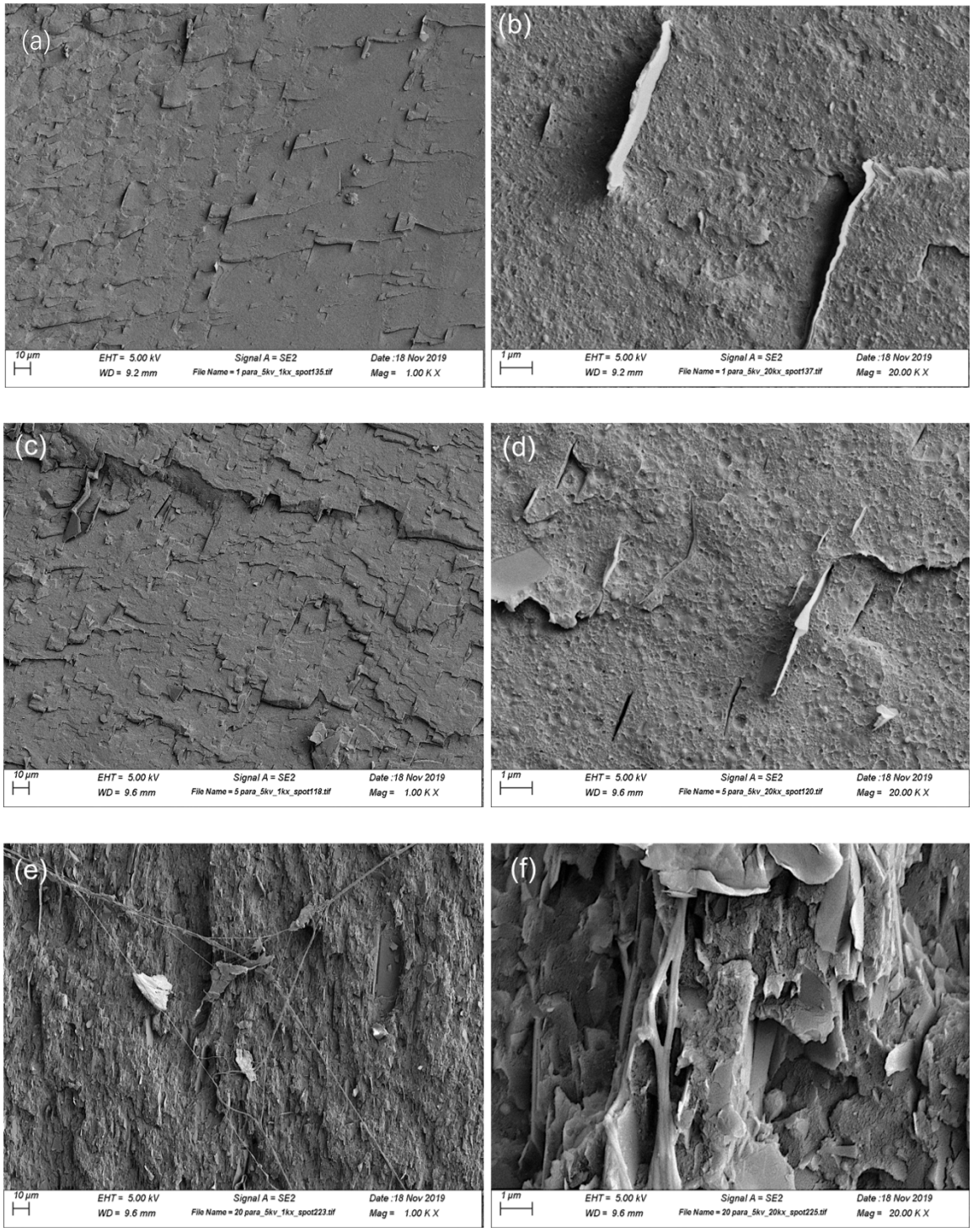

Figure 3.4 SEM micrographs of the GNF-ABS composites at 10 µm and 1 µm scales: 1GNF-ABS (a, b), 5GNF-ABS (c, d), and 20GNF-ABS (e, f).

3.5 Electrical Test Results

During electrical conductivity testing, the signal was very noisy for 1 and 5 wt. % GNFs in ABS, indicated low electrical conductivity. However, at 20 wt. % GNFs in ABS, electrical conductivity was measured and conductivity-voltage curves are shown in Figure 3.5. Conductivity increases with voltage until about 200 V, after which conductivity decreases. Results show that the specimen take from position C had the highest conductivity, and position A had the lowest conductivity. Thus, electrical conductivity varies with position along the length of the injection molded part. Electrical conductivity increases along the specimen length, where position A is closest to where the material enters the mold.

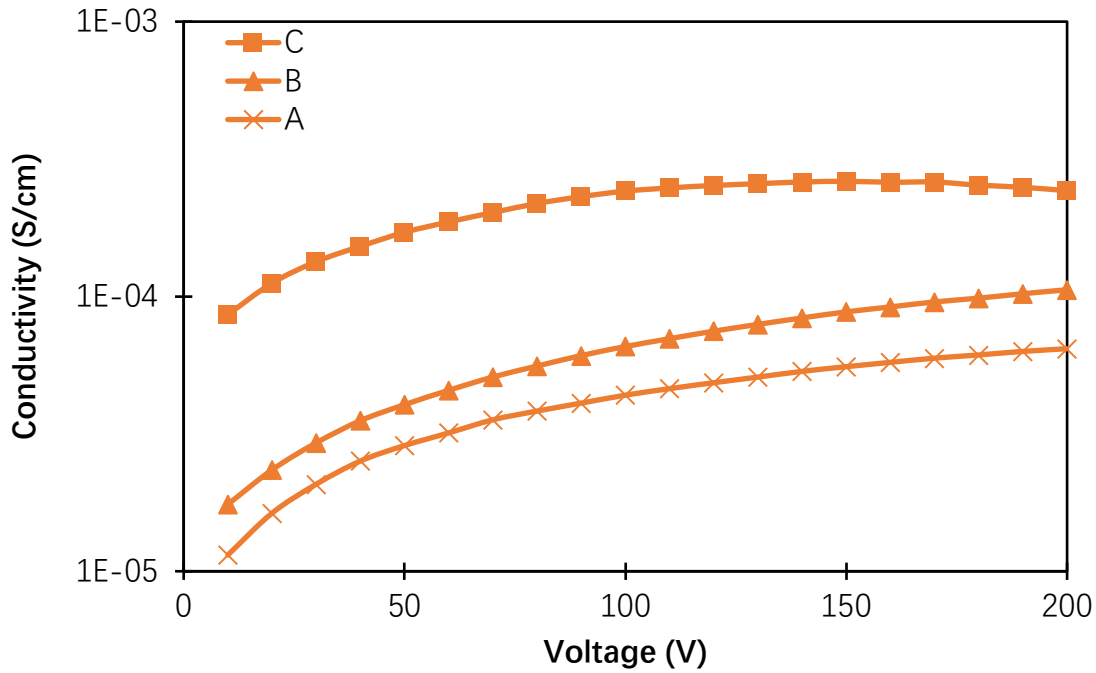

Figure 3.5 Conductivity-voltage curves for A, B, and C parts of 20 wt.% GNF in ABS.

3.6 Flexural Test Results

Flexural stress-strain curves are shown in Figure 3.6. Comparing the three GNF concentrations, 20 wt.% GNFs in ABS has the highest flexural strength. The average flexural modulus of the G-ABS is shown in Figure 3.7. Flexural modulus increases from 2.38 GPa to 8.95 GPa with GNF increase from 1 % to 20 %. These results indicate that flexural strength and modulus increased with increasing GNF concentration in ABS, and flexural modulus increases linearly with GNF concentration between 1 and 20 wt. %.

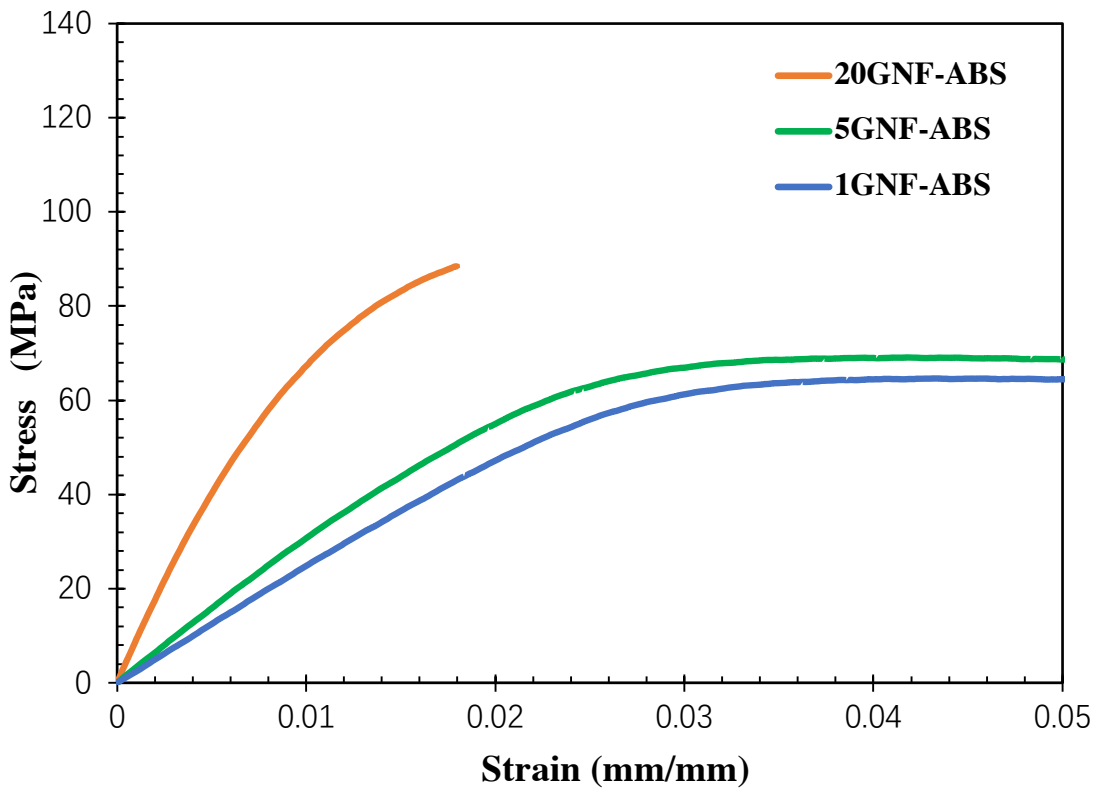

*Figure 3.6 S*tress-strain curves for 1, 5, and 20 wt.% GNFs in ABS

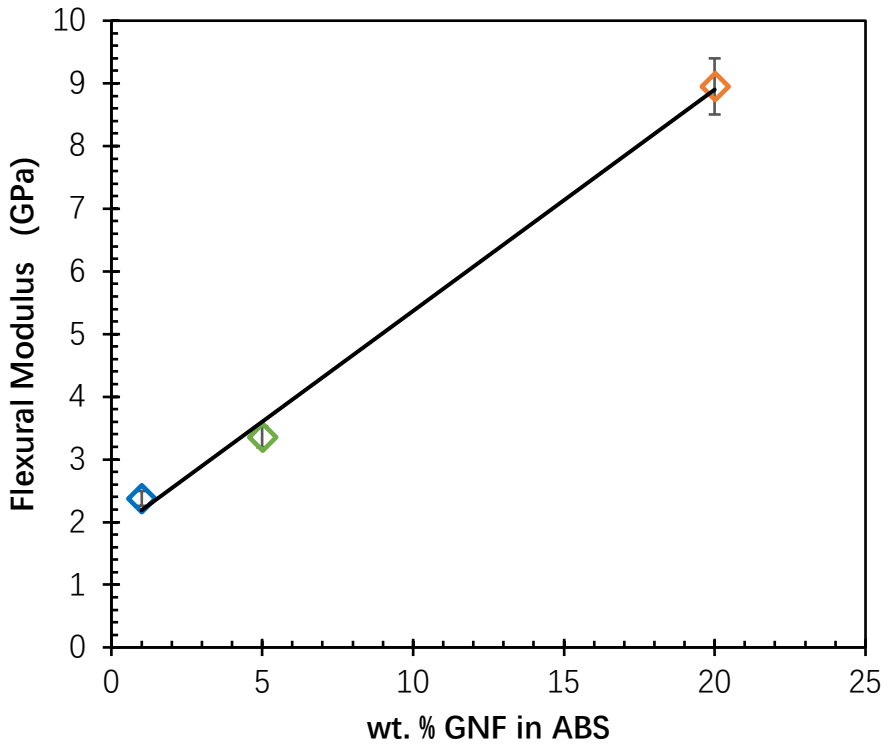

Figure 3.7 Average flexural modulus for 1, 5, and 20 wt.% GNFs in ABS.

4 Chapter 4: Conclusions

GNF reinforced ABS nanocomposites were prepared by shear exfoliation of graphite into GNFs directly within ABS at 1, 5, and 20 wt. % GNFs in ABS followed by injection molding to fabricate test specimens.

Raman results indicate that GNFs are multi-layer graphene in GNF-ABS composites, while XRD results indicate over eighty layers in the GNFs on average. Raman technology can detect GNFs oriented in all directions, but from the Bragg's law, XRD can only study GNFs oriented properly in the (002) direction. Thus, we suggest that oriented GNFs parallel to the specimen surface have a higher number of layers on average than GNFs randomly oriented. Graphite exfoliation into GNFs appears to be more efficient with increasing graphite concentration, as indicated by the decreased number of layers in each GNF particle found in the XRD results and by the decreased point defects indicated in the XPS results.

Mechanical properties increase significantly with increasing GNF concentration in ABS, including flexural modulus and strength. This significant increase in mechanical properties is supported by the resulting morphology of the GNF-ABS nanocomposites. SEM micrographs shows good GNF distribution within ABS and good particle-matrix interaction between GNF and ABS, which enable efficient load transfer when a load is applied.

With high GNF concentration (i.e. 20 wt. % GNFs in ABS) coupled with uniform GNF distribution with the matrix, the GNFs impart electrical conductivity. With increasing

GNF concentration, electrical conductivity is expected to increase further. Interestingly, electrical conductivity of the specimen is dependent upon location along the specimen length. Electrical conductivity increases along the flow direction of the injection molded specimen.

Future work will include a more detailed analysis of XPS results to determine bonding between GNFs and ABS, as well as why electrical conductivity increases along the length of the molded specimen. A future study will involve sectioning the molded specimen at positions A, B, and C followed by XRD, Raman, and SEM analysis of each location to determine morphological and structural differences at these three positions.

This research demonstrates the use of GNF enhancement to generate ABS nanocomposites with easily tunable properties, including electrical conductivity and mechanical properties. Graphite exfoliation into GNFs provides mechanical property enhancements on par with chopped carbon fiber reinforcement. However, since the starting material is graphite, rather than graphene or carbon fiber, GNF-ABS composites are low cost. GNF-ABS composites may be processed using any standard polymer processing method, including extrusion, injection molding, additive manufacturing, etc, which all support mass production of complex shapes. The low cost of this technology, the multifunctional, tunable properties, and facile part fabrication of GNF-ABS composites make this a suitable technology for a wide array of industrial applications.

References

[1] Shenavar A, Abbasi F. Morphology, thermal, and mechanical properties of acrylonitrile–butadiene–styrene/carbon black composites. Journal of Applied Polymer Science. 2007;105(4):2236-2244.

[2] Mayasari HE, Setyorini I, Yuniari A. Thermal degradation and swelling behaviour of acrylonitrile butadiene styrene rubber reinforced by carbon black. . 2018;432(1).

[3] Jyoti J, Dhakate SR, Singh BP. Phase transition and anomalous rheological properties of graphene oxide-carbon nanotube acrylonitrile butadiene styrene hybrid composites. Composites Part B: Engineering. 2018;154:337-350.

[4] Mari D, Schaller R. Mechanical spectroscopy in carbon nanotube reinforced ABS. Materials Science and Engineering: A. 2009;521-522:255-258.

[5] Ben Difallah B, Kharrat M, Dammak M, Monteil G. Mechanical and tribological response of ABS polymer matrix filled with graphite powder. Materials and Design. 2012;34:782-787.

[6] Heo C, Moon H, Yoon CS, Chang J. ABS nanocomposite films based on functionalized ‐ graphene sheets. Journal of Applied Polymer Science. 2012;124(6):4663-4670.

[7] Dul S, Fambri L, Merlini C, et al. Effect of graphene nanoplatelets structure on the properties of acrylonitrile–butadiene–styrene composites. Polymer Composites. 2019;40:E285-E300.

[8] Caradonna A, Colucci G, Giorcelli M, Frache A, Badini C. Thermal behavior of thermoplastic polymer nanocomposites containing graphene nanoplatelets. J Appl Polym Sci. 2017;134(20).

[9] Singh R, Sandhu GS, Penna R, Farina I. Investigations for thermal and electrical conductivity of ABS-graphene blended prototypes. *Materials*. 2017;10(8).

[10] U.S. patent #133229, dated 19 November 1872.

[11] Merril, Arthur M. (1955). Plastics Technology, Volume 1. Rubber/Automotive Division. of Hartman Communications, Incorporated, 1955.

[12] Torr, James (11 April 2010). "A Short History of Injection Moulding". AV Plastics. Injection Moulding - Get Stuff Made

[13] Injection Molding Handbook (2nd ed.).

[14] P. Scherrer, Göttinger Nachrichten Gesell., Vol. 2, 1918, p 98.

[15] Strankowski M, Wlodarczyk D, Piszczyk L, Strankowska J. Polyurethane. nanocomposites containing reduced graphene oxide, FTIR, raman, and XRD studies. Journal of Spectroscopy. 2016.

[16] Feng H, Wang X, Wu D. Fabrication of spirocyclic phosphazene epoxy-based. nanocomposites with graphene via exfoliation of graphite platelets and thermal curing for enhancement of mechanical and conductive properties. Industrial & Engineering Chemistry Research. 2013;52(30):10160-10171.

[17] Key words. Journal of the American Academy of Child & Adolescent Psychiatry.

2017;56(10):xii-xiii.

[18] J. F. Watts and J. Wolstenholme, An Introduction to Surface Analysis by XPS and. AES (2003).

[19] D. Woodruff and T. Delchar, Modern Techniques of Surface Science (1994).

[20] Suzuki, E. (2002). "High-resolution scanning electron microscopy of immunogold-labelled cells by the use of thin plasma coating of osmium". Journal of Microscopy. 208 (3): 153–157.

[21] Goldstein J.I. et al. (2003) Generation of X-Rays in the SEM Specimen. In: Scanning Electron Microscopy and X-ray Microanalysis. Springer, Boston, MA.

[22] What Is a Source Measure Unit (SMU), National Instruments, retrieved July 11, 2016.

[23] ASTM standards D257.

[24] Pang X, Shi X, Kang X, Duan M, Weng M. Preparation of boratemodified expandable graphite and its flame retardancy on acrylonitrile-butadiene-styrene resin. Polymer Composites. 2016;37(9):2673-2683.